

FIELD OBSERVATIONS AND NUMERICAL EXPERIMENTS TO ASSESS THE EFFECT OF TREES ON SLOPE STABILITY

Wei-Li Liang^{1*}, Ken'ichirou Kosugi², Takahisa Mizuyama³, Yoshiiku Musashi⁴

ABSTRACT

To clarify the effect of trees on soil water dynamics and slope stability, we conducted field observations and numerical simulations of rainwater infiltration processes on a forested hillslope. The results of field observations indicated that locally concentrated rainwater input attributable to stemflow on the downslope side of the tree trunk caused the large and rapid increases in water content and pore water pressure in the region downslope of the tree stem, resulting in the development of an asymmetric saturated zone around the tree. Rainwater infiltration simulations were conducted with the proposed model (Liang *et al.*, 2009), in which stemflow was parameterized as a source flux spring in soil layers, and the conventional model, in which rainwater concentrated by the stemflow was disregarded. The simulation results were then used for the slope stability analysis. The proposed model resulted in the timing of minimum safety factor < 1.0 at an earlier stage than in the conventional model. Furthermore, the proposed model showed evidence of the risk for slope failure throughout all parts of the slope. However, the conventional model showed only the risk of slope failure in the lower part of the slope.

Key Words: Numerical simulation, Saturated zone, Slope stability, Stemflow

INTRODUCTION

Precipitation in a forest is intercepted by the canopy and is partitioned into throughfall and stemflow, as diffuse input and point input, respectively, so that the water reaching to forest floor is not uniform. Ford and Deans (1978) and Durocher (1990) observed very rapid water movement underneath trees and indicated that this kind of rapid soil water movement was primarily controlled not by variability in soil physical properties but rather by small-scale spatial variability in the water input to the soil surface. Thus, trees have a major impact on water movement in soil because of rainfall redistribution processes. Although there are many numerical models that consider the division of precipitation into interception and throughfall components (e.g., Bouting *et al.*, 1992; Keim *et al.*, 2006), the rainwater concentrated by stemflow has generally been disregarded. Liang *et al.* (2009) developed the rainwater infiltration model which considers stemflow as a source flux spring in soil layers. The simulation results showed adequate spatial and temporal variations in soil water dynamics and closely agreed with observed data. However, simulations using the conventional net precipitation input assumption, in which rainwater concentrated by stemflow is disregarded,

1 Postdoctoral Researcher, Graduate School of Agriculture, Kyoto University, Kyoto 606-8502, Japan.

(*Corresponding Author; Tel.: +81-75-753-6091; Fax: +81-75-753-6088; Email: iritu@kais.kyoto-u.ac.jp)

2 Associate Professor, Graduate School of Agriculture, Kyoto University, Kyoto 606-8502, Japan.

3 Professor, Graduate School of Agriculture, Kyoto University, Kyoto 606-8502, Japan.

4 Deputy Section Manager, Water Resources Dep., Yachiyo Engineering Co., Ltd., Tokyo 161-8575, Japan.

showed an even downward expansion of the wetting front into the soil, contradicting the observed data. This suggests that the conventional models used in previous studies do not represent the spatial variations in soil water dynamics and are likely to contain significant errors in the prediction of slope failure. The purpose of this study was to clarify the effect of trees on soil water dynamics and slope stability, based on field observations and numerical simulations. To simulate soil water dynamics around trees on the hillslope, rainwater infiltration simulations were conducted with the proposed model (Liang *et al.*, 2009) and the conventional model. The simulation results were then used for the slope stability analysis.

FIELD OBSERVATIONS

Methods and materials

Observations were conducted on a hillslope at the Kamigamo Experimental Station of Kyoto University, located in southern Kyoto Prefecture, central Japan ($35^{\circ}04'N$, $135^{\circ}46'E$). The hillslope has a mean gradient of 28 degrees, with brown forest soil classified as Cambisol underlain by sandstone and slate. It is predominantly covered with tall stewartia (*Stewartia monadelpha*), planted in 1956.

To monitor soil water dynamics around a tree, we selected a tall stewartia and delineated a longitudinal observation line from upslope to downslope of this tree. We installed capacitance meters (Sentek, EasyAG-5p) and tensiometers at each of ten points: 250 cm (P1), 200 cm (P2), 150 cm (P3), 100 cm (P4), and 50 cm (P5) upslope from the tree stem and 25 cm (P6), 50 cm (P7), 100 cm (P8), 150 cm (P9), and 200 cm (P10) downslope from the tree stem. Each capacitance meter consisted of five sensors to measure soil water content at depths of 10, 20, 30, 40, and 50 cm. Tensiometers installed at the soil–bedrock interface were used to monitor saturated zone occurrences at the soil–bedrock interface. These equipments were used to monitor the process of rainfall infiltration from the soil surface through the soil–bedrock interface. Furthermore, we selected another tall stewartia to measure stemflow. To separately collect stemflow data upslope and downslope of the tree trunk, we used two tubes cut longitudinally and wrapped spirally around the upslope and downslope sides of the trunk. The flow rates of stemflow upslope and downslope of the tree trunk were measured using tipping-bucket gauges, respectively.

Results and discussion

Figure 1 shows the rainfall, stemflow measured on the downslope side of the trunk (SF-down), and spatial variation in soil water content change ($\Delta\theta$) and hydraulic head (ϕ) for the storm event on 25 May 2007 (accumulated rainfall: 62 mm). The distribution of $\Delta\theta$ clearly indicates where the water brought by the storm event was stored (Fig. 1b). For ϕ values greater than the soil–bedrock interface, the generation of positive pore water pressure is indicated (Fig. 1c). At 50 min (accumulated rainfall: 3 mm, accumulated SF-down: 0.5 L), $\Delta\theta$ obviously increased at P6, especially at 50 cm depth where rapid and great response was measure ($\Delta\theta = 0.15$). At the same time, ϕ at P6 became higher than the height of the soil–bedrock interface, indicating the generation of a saturated zone. No obvious changes in $\Delta\theta$ and ϕ were observed at the other points. At 280 min (accumulated rainfall: 15 mm, accumulated SF-down: 57 L), $\Delta\theta$ increased greatly at P6 and P7, whereas the increases of $\Delta\theta$ at other points were limited to the upper soil layers from 0 to 20 cm. Saturated zones were formed at P6 and P7, whereas there were no changes in ϕ at the other points. At 570 min (accumulated rainfall: 34 mm, accumulated

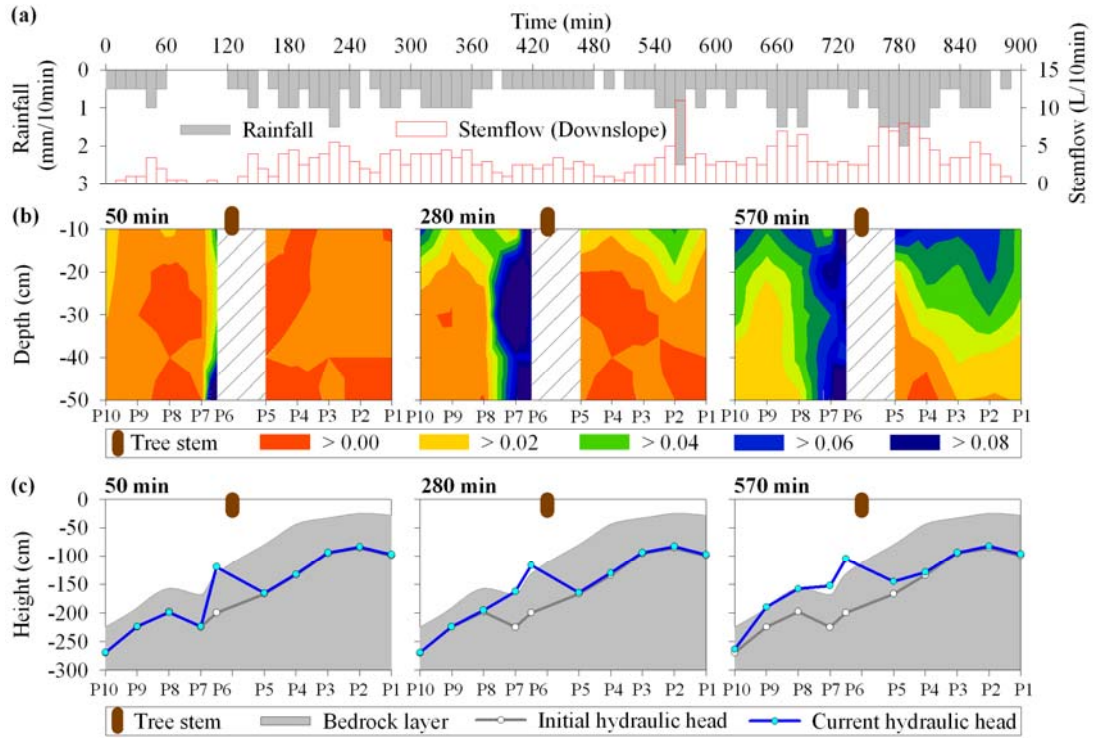


Fig. 1 (a) Hyetograph and stemflow measured on the downslope side of the tree, and spatial variation in (b) soil water content change and (c) hydraulic head at 50 min, 280 min, and 570 min for the rainfall event on 25 May 2007. Soil water content change is defined as the difference between the current water content and the initial water content observed at the start of the storm event. Hydraulic head is computed as the sum of the observed pressure head and the height of the soil–bedrock interface (elevation head). Initial hydraulic head in Fig. 1c is the hydraulic head observed at the start of the storm event.

SF-down: 145.5 L), rainfall and SF-down intensities reached the maximum (2.5 mm and 11 L per 10 min, respectively) for the event. Increases in $\Delta\theta$ were observed at all depths for each point, and high $\Delta\theta$ at P6 and P7 were similar to that observed at 280 min. In the downslope region, ϕ values rose to near or above the bedrock surface at P6–P9, especially high ψ values were recorded at P6 (26.4 cm) and P7 (15.8 cm). There were no obvious changes in ϕ changes at P1–P4 in the upslope region. At P5, the increase in ϕ could be attributed to occurrence of water flow toward the upslope direction but to rainwater from vertical infiltration due to little increases in $\Delta\theta$ at depths lower than 30 cm.

The rapid propagation of infiltrated water caused the significant generation of a saturated zone at the points closest to the tree in the downslope region but not in the upslope region, resulting in an asymmetrically distributed saturated zone and an expansion of a saturated zone from the downslope to the upslope region around the tree. Thus, soil water dynamics did not depend simply on the distance from the tree but was significantly different between the upslope and downslope regions. The same tendency was also observed in many events (Liang *et al.*, 2007), which was the result of stemflow concentrated on the downslope side of the tree. For the storm event shown in Fig. 1a, stemflow on the downslope side of the tree was 99% of total stemflow. It was likely caused by the uneven area between the upslope and downslope sides of the canopy and by asymmetrical stemflow pathways between the upslope and downslope sides of the trunk due to downslope tilting of the tree trunk. We presume that this asymmetrical generation of stemflow probably occurs in general on trees growing on a hillslope and thus has important implications for hillslope hydrological processes and slope stability.

NUMERICAL EXPERIMENTS

As the field observation results described above, stemflow serving as point input to the forest floor could have great implications for soil water dynamics as well as slope stability. Thus, simulations using the conventional model disregarding rainwater concentrated by the stemflow are likely to contain large errors. In numerical experiments follows, we conducted rainwater infiltration simulations with the model (Model 1) proposed by Liang *et al.* (2009), in which stemflow was parameterized as a source flux spring in soil layers, and the conventional model (Model 2), in which rainwater concentrated by the stemflow was disregarded. The simulation results were then used for the slope stability analysis.

Numerical modeling methods: two-dimensional rainwater infiltration simulations and slope stability analysis

To simulate water flow in the soil layers, the two-dimensional Richards equation was solved using the finite element method:

$$C(\psi) \frac{\partial \psi}{\partial t} = \frac{\partial}{\partial x} \left[K(\psi) \left(\frac{\partial \psi}{\partial x} \right) \right] + \frac{\partial}{\partial z} \left[K(\psi) \left(\frac{\partial \psi}{\partial z} \right) + 1 \right] + S \quad (1)$$

where ψ (cm) is water pressure head, t (s) is time, x (cm) and z (cm) are the longitudinal and vertical (positive upward) directions, respectively; and S (cm^2) is a source–sink term that is positive as a source and negative as a sink. The quantity $C(\psi)$ (cm^{-1}) is the soil water capacity function, and $K(\psi)$ (cm s^{-1}) is the hydraulic conductivity function, which are related to soil hydraulic properties. Typical weathered granite soil properties were assumed and soil hydraulic parameters reported in the previous study (Liang *et al.*, 2006) were used because granite soils are known to be very sensitive to weathering and vulnerable to landslides.

Numerical experiments were set up in a forested catchment consisting of a stream channel and symmetrical sidewall hillslopes (Fig. 2a). Within the site, a sidewall hillslope with a gradient of 50° and a soil depth of 1 m was used for rainwater infiltration simulations (Fig. 2b). Three trees were present on the hillslope, corresponding to a planting rate of 900/ha. A two-dimensional calculation domain, divided by the triangle finite element mesh, comprised

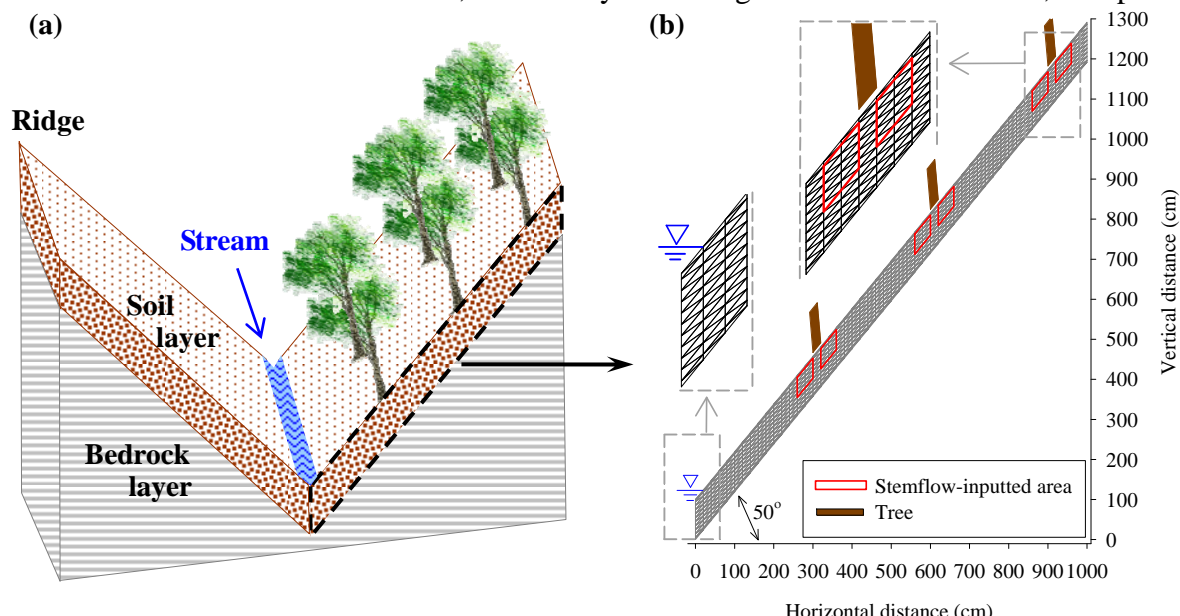


Fig. 2 (a) Sideslope and stream systems, and (b) two-dimensional calculation domain divided by the finite element for the infiltration simulation and slope stability.

612 nodes and 1100 elements (Fig. 2b). The downslope boundary adjoining the opposite sidewall slope corresponds to the center of the stream channel, where the constant water level was set 23.8 cm above the boundary. The bottom and upslope boundaries correspond to the soil–bedrock interface and ridge of the hillslope, respectively. On the downslope, bottom, and upslope boundaries, no-flux boundary conditions were imposed. On the surface boundary, seepage face boundary conditions were imposed. The initial condition of ψ for the main simulations was determined using a preparatory calculation in which the initial ψ value of -50 cm was assigned to each node, and a precipitation rate of 20 mm/h was stably applied to the surface for 1 day. All ψ values at 2 days after the end of applied rainfall were defined as initial ψ for the main simulations, corresponding to the dried steady state. The settings above correspond to those used by Sammori and Tsuboyama (1990) and Mukhlisin *et al.* (2006).

Precipitation rates of 30 mm/h were stably applied to Model 1 and Model 2. The amounts of throughfall, stemflow, and interception were set as 50%, 30%, and 20% of the total precipitation. Stemflow generated on the downslope side of a stem was assumed to be 80 times greater than on the upslope side. In Model 1, throughfall was evenly inputted across the surface boundary, except in the tree stem area (Fig. 2b). Stemflow on the upslope and downslope sides of a tree were inputted to source regions (Fig. 2b). In Model 2, the net precipitation (sum of throughfall and stemflow, i.e., 80% of precipitation) was evenly inputted across the soil surface area, except in the tree stem area. The total amounts of inputted stemflow and throughfall in Model 1 were the same as those in Model 2.

Slope stability analysis was conducted using the Bishop method (Bishop, 1955), in which the safety factor (F_s) is computed based on the moment equilibrium among slices in a sliding circle:

$$F_s = \frac{1}{\sum W_i \sin \alpha_i} \sum \left[\frac{c_i b_i + (W_i - u_i b_i) \tan \phi_i}{(1 + \tan \alpha_i \tan \phi_i / F_s) \cos \alpha_i} \right] \quad (2)$$

where u_i (cm) is the positive pore water pressure at the bottom of the slice i , W_i (g) is the weight of the slice i , b_i (cm) is the horizontal length of the slice i , α_i ($^{\circ}$) is the slope of the bottom of the slice i , ϕ_i ($^{\circ}$) is the internal frictional angle, and c_i is the cohesion (gf cm^{-2}). As suggested by Sammori and Tsuboyama (1990), the cohesion c_i was assumed to be dependent on the negative pore water pressure u'_i (cm) and the degree of saturation ($\theta/\theta_{s,i}$):

$$c_i = c'_i - \chi u'_i \tan \phi_i, \quad \chi = \min \left(1.25 \frac{\theta_i}{\theta_{s,i}}, 1 \right) \quad (3)$$

where c'_i (gf cm^{-2}) is the cohesion in the saturated condition. The values of u_i , W_i , and c_i were computed for each time step from the pore water pressures and soil moisture contents as simulated by Model 1 and Model 2. For calculating F_s , the total number of slices i was fixed at a value of 10. By changing the center and the radius of circular arcs within the preset region, the values of sliding circular arcs were tested to determine the minimal F_s ($\text{Min}F_s$) at each time step. Furthermore, values of $c'_i = 20$ (gf cm^{-2}), $\phi_i = 35$ ($^{\circ}$), solid density = 2.65 (g cm^{-3}) were assigned, as suggested by Suzuki (1991) and Mukhlisin *et al.* (2006) as typical values for a weathered granite soil. Because the study assumed that plantings consisted of a shallow-rooted tree, the shear force of roots on the soil–bedrock interface was disregarded.

Effects of stemflow infiltration on slope stability

Figure 3 shows the spatial variations in ψ as simulated using Model 1 and Model 2. The distribution of ψ clearly indicates where the wetting front expanded. At 0 min (the initial

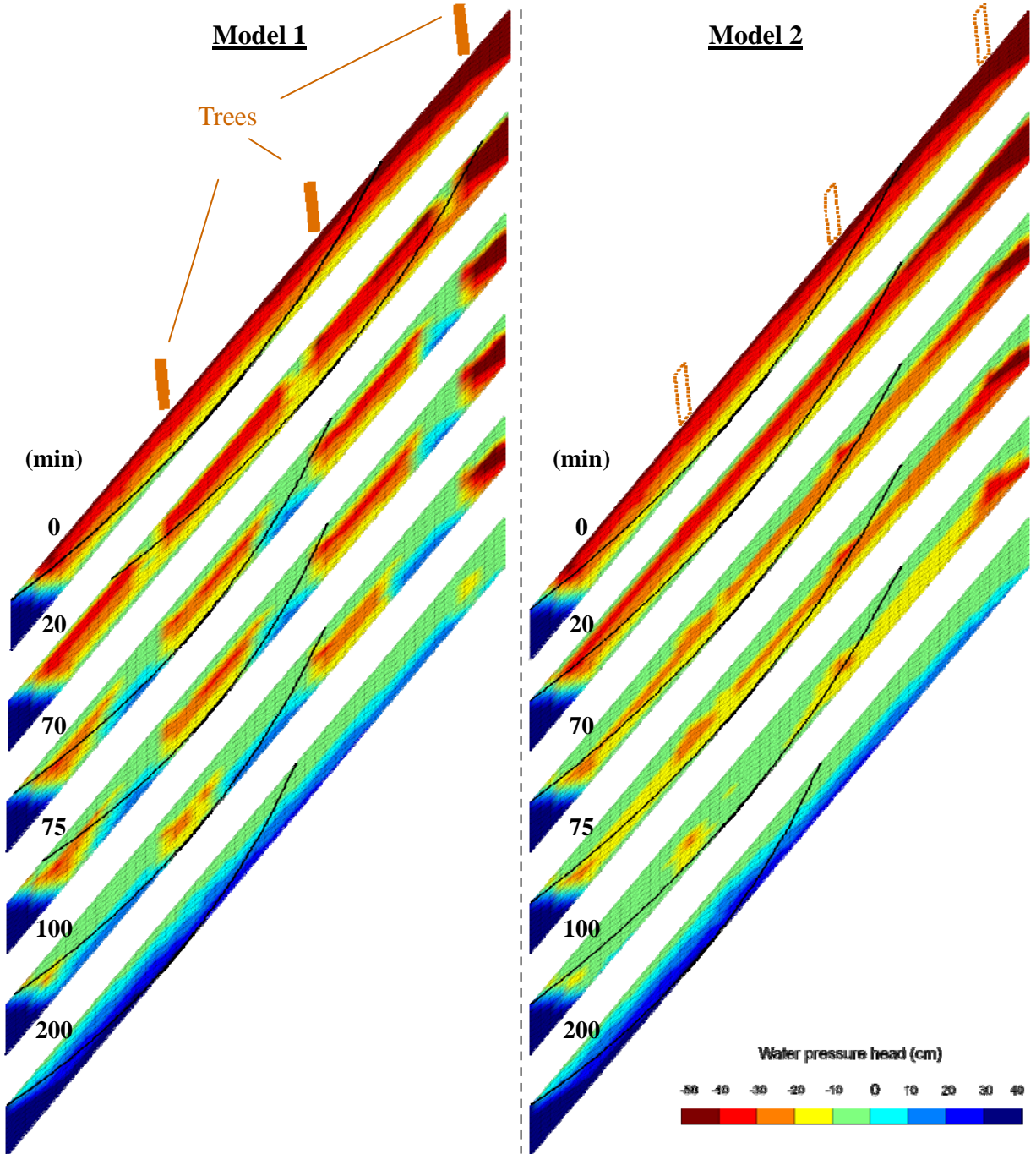


Fig. 3 Two-dimensional view of spatial variations in water pressure head, simulated using Model 1 and Model 2 after 0, 20, 70, 75, 100, 200 min of the applied rainfall. The arc in each panel is the sliding arc with minimum safety factor at the time.

condition), the dried steady state of a saturated zone was present only in the downslope region, corresponding to the stable water level of the stream (Fig. 2b). At 20–100 min, Model 1 showed a rapid infiltration of rainwater at locations downslope of the trees, where the creation of saturated zones was simulated. In contrast, Model 2 showed an even-downward expansion of the wetting front and no obvious generation of a saturated zone. At 200 min, a wetted steady state was created, in which a significant saturated zone was simulated from downslope to upslope in Model 1 and Model 2. From 0 to 200 min, clear differences were evident in the generation processes of saturated zones between Model 1 and Model 2 before onset of the wetted steady state. Therefore, Model 1 properly represented the asymmetric generation of a

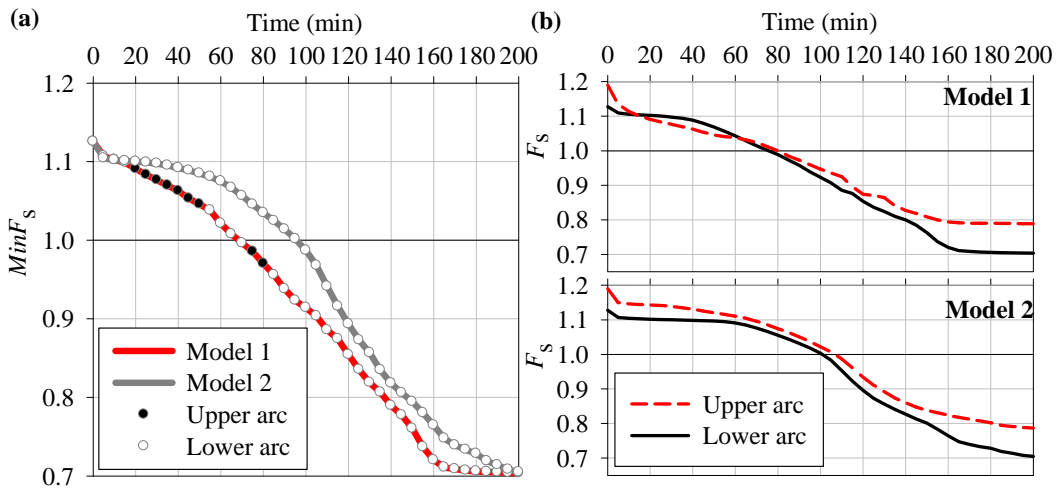


Fig. 4 (a) Temporal changes in the minimum safety factor ($\text{Min}F_s$) and (b) Temporal changes in safety factor (F_s) calculated at the location of the upper arc and the lower arc for infiltration simulations with Model 1 and Model 2. In Fig. 4a, $\text{Min}F_s$ calculated from all sliding arcs were sorted by upper arcs (black circle symbols) and lower arcs (white circle symbols). In Fig. 4b, the upper arc corresponds to the sliding arcs calculated at 20 min for Model 1, and the lower arc corresponds to the sliding arcs calculated at 200 min for Model 1 as well as Model 2 shown in Fig. 3.

saturated zone around the trees. In contrast, Model 2 exhibited a slow and even expansion of the wetting front at all points, in contradiction with the observations. $\text{Min}F_s$ for Model 1 clearly decreased more rapidly and was smaller than that for Model 2 before the wetted steady state (Fig. 4a). At 70 min in Model 1, the greater generation rates of saturated zones were simulated downslope of trees (Fig. 3) and $\text{Min}F_s$ was less than 1.0 (Fig. 4a), indicating slope failure. At this time, Model 2 showed no generation of saturated zones around trees, and $\text{Min}F_s$ was greater than 1.0. Model 2 showed $\text{Min}F_s < 1.0$ at 100 min, indicating a prediction of slope failure in Model 2 at 30 min later than when slope failure occurred in Model 1.

Figure 3 presents the locations of the sliding arcs with $\text{Min}F_s$ calculated for both Model 1 and Model 2. All sliding arcs are classified into lower arcs and upper arcs, in which the lower arc is defined as a sliding arc occurring adjacent to the water level in the downslope, indicating slope failure occurring on the lower part of the slope, and in which the upper arc is defined as a sliding arc occurring above the water level in the downslope, indicating slope failure occurring on the middle or upper part of the slope. The locations of the sliding arcs varied more significantly in Model 1 than in Model 2 due to the variable rates of saturated zone generation at the soil–bedrock interface in Model 1. Additionally, three upper arcs were calculated at 20, 75, and 80 min in Model 1, but not in Model 2, in which only the lower arcs were determined. To clarify the potential risk of slope failure at the location of the lower and upper arcs, temporal changes in F_s at the location of the upper arc at 20 min in Model 1 (Fig. 3) and the lower arc at 200 min in Model 1 as well as in Model 2 (Fig. 3) were calculated for both Model 1 and Model 2. In Model 1 (Fig. 4b), F_s value of the upper arc decreased rapidly and significantly and exhibits the less F_s than the lower arc at 15–60 min. This suggests that the potential for slope failure exists not only in the lower part but also in the middle and upper parts of the slope. In Model 2 (Fig. 4b), however, F_s of the lower arc was always less than in the upper arc, indicating that only slope failure from the lower part of the slope could be predicted with this model.

In summary, Model 1 exhibits more rapid decreases in minimum F_s than Model 2, causing the timing of reaching $\text{Min}F_s < 1.0$ to be earlier in Model 1 than in Model 2. For spatial variations, Model 1 shows variable sliding arcs including both types of lower and upper arc, indicating

the potential risk of slope failure from all parts of the slope. However, Model 2 shows the failure in the lower arc as well, consistent with results in previous studies (Sammori and Tsuboyama, 1990; Mukhlisin *et al.*, 2006), and indicates that only slope failure from the lower part of the slope could be predicted in this model. This further suggests that the concentrated infiltration characteristics of stemflow would significantly affect the timing and location of slope failure. Moreover, large spatiotemporal errors clearly exist in the predictions of slope failure in previous studies using conventional assumptions of rainwater inputs.

Influences of different topographic and meteorological conditions on slope stability

Topographic and meteorological conditions can affect slope stability. To clarify the effect of stemflow infiltration on slope stability under the different situations, simulations using Model 1 were conducted under various conditions of slope gradient, soil depth, and stemflow rates. Except for conditions used for comparison, other settings were the same in all cases. Figure 5 shows the slope stability analysis for Model 1 under slope gradients of 40°, 50°, and 60°. For temporal variations (Fig. 5a), $MinF_s$ decreased with increases of slope gradients. For spatial variations (Fig. 5b), some upper arcs were calculated at the slope gradients of 50° and 60°, but 40°, in which only the lower arcs were determined. These results suggest that the slope gradient contributes positively to slope failure and enlarges the potential risk of slope failure occurring in the middle to upper parts of the slope. Figure 6 shows the slope stability analysis for Model 1 under soil depths of 60, 100, and 140 cm. For temporal variations (Fig. 6a), $MinF_s$ decreased significantly with decreases in soil depths. For spatial variations (Fig. 6b), some upper arcs were calculated at soil depths of 60 and 100 cm, but 140 cm, in which only the lower arcs were determined. These results suggest that soil depth contributes negatively to slope failure and reduces the potential risk of slope failure occurring in the middle and upper parts of the slope. Figure 7 shows slope stability analyses for Model 1 under stemflow rates of 10%, 30%, and 40% of the total precipitation. In all cases, the net precipitation was fixed at 80% of the total precipitation. For temporal variations (Fig. 7a), $MinF_s$ decreased significantly with increases in stemflow rates. For spatial variations (Fig. 7b), the upper arc was calculated in all cases, even under a small stemflow rate of 10% of the total precipitation. These results suggest that stemflow contributes positively to slope failure.

In summary, stemflow infiltration may have major implications for slope stability, even for tree species with a low proportion of stemflow to precipitation. The effect of stemflow

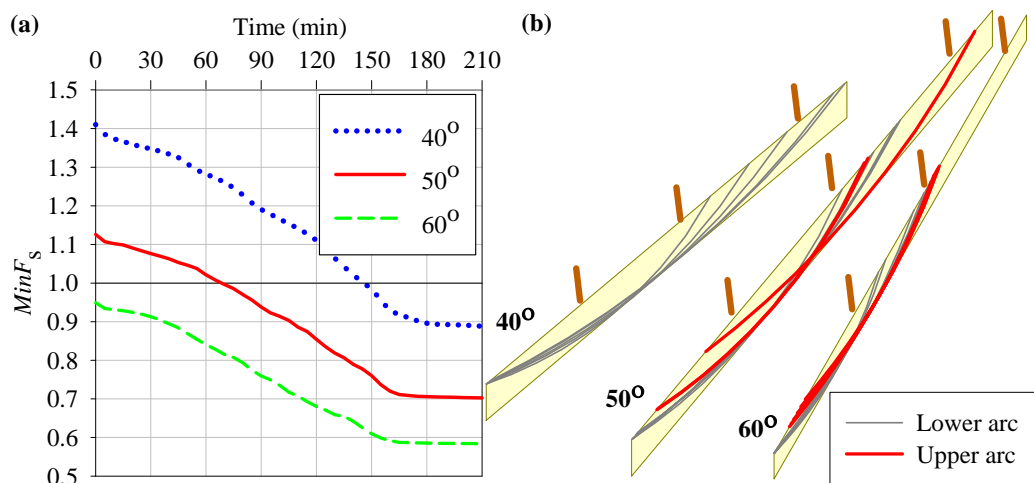


Fig. 5 (a) Temporal changes in minimum safety factor ($MinF_s$) and (b) locations of all sliding arcs for infiltration simulations with Model 1 for different slope gradients of 40°, 50°, and 60°.

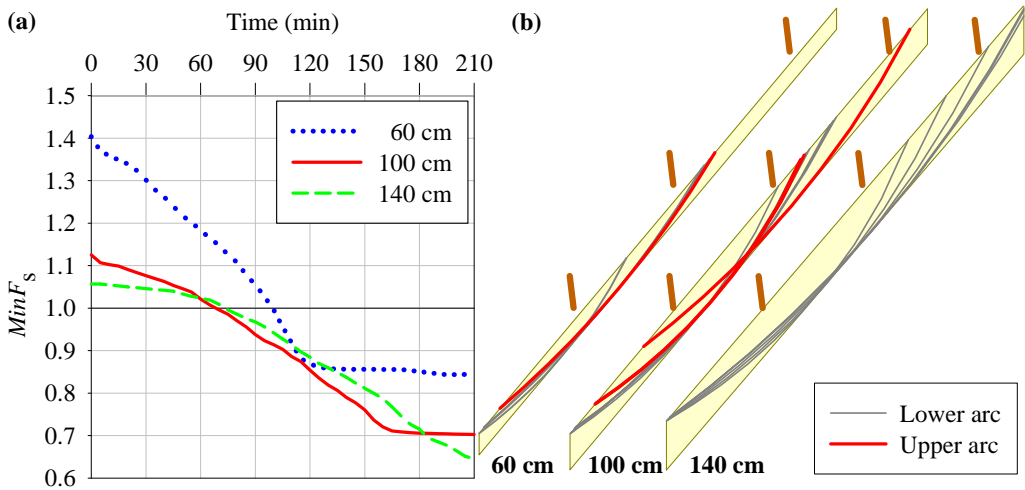


Fig. 6 (a) Temporal changes in minimum safety factor ($MinF_s$) and (b) locations of all sliding arcs for infiltration simulations with Model 1 for different soil depths of 60, 100, and 140 cm.

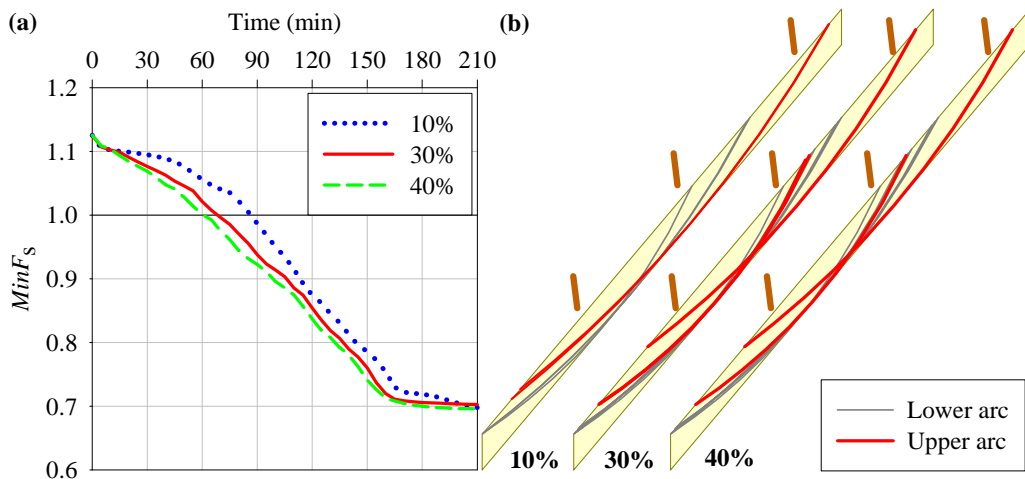


Fig. 7 (a) Temporal changes in minimum safety factor ($MinF_s$) and (b) locations of all sliding arcs for infiltration simulations with Model 1 for different stemflow rates of 10%, 30%, and 40% of the total precipitation.

infiltration on slope failure could be greater for slopes with greater gradients or lesser soil depth, increasing the risk of slope failure throughout all parts of the slope. On slopes with smaller gradients or greater soil depths, however, the effect of stemflow infiltration would be less, and slope failure would only occur in the lower part of the slope.

CONCLUSIONS

To clarify the effect of trees on soil water dynamics and slope stability, we conducted field observations and numerical simulations of rainwater infiltration processes on a forested hillslope. The results of field observations indicated that locally concentrated rainwater input attributable to stemflow on the downslope side of the tree trunk caused the large and rapid increases in water content and pore water pressure in the region downslope of the tree stem, resulting in the development of an asymmetric saturated zone around the tree.

The slope stability analysis was conducted for rainwater infiltration simulations with the proposed model (Liang *et al.*, 2009), considering the characteristic of stemflow infiltration,

and the conventional model, using the conventional net precipitation input assumption. The proposed model shows more rapid decreases in the minimum safety factor ($MinF_s$) attributable to greater generation rates of saturated zones downslope of trees. This model also results in the timing of $MinF_s < 1.0$ at an earlier stage than in the conventional model. Furthermore, the proposed model shows evidence of the risk for slope failure throughout all parts of the slope. However, the conventional model shows only the risk of slope failure in the lower part of the slope, and clearly indicates the effect of concentrated stemflow infiltration on the timing and location of slope failure. This model also suggests that large spatiotemporal errors exist in the prediction of slope failure in previous studies using conventional assumptions of rainwater inputs. The effect of stemflow on slope stability would be greatest in slopes with steeper gradients or shallower soil depths, where the risk of slope failure exists in all sections of the slope. On slopes with smaller gradients or greater soil depths, however, the effects of stemflow infiltration would be lessened, where slope failure would only occur in the lower part of the slope.

REFERENCES

- Bishop, A.W. (1955). "The use of the slip circle in the stability analysis of slopes," *Geotechnique*, 5(1): 7-17.
- Bouten, W., Schaap, M.G., Bakker, D.J. and Verstraten, J.M. (1992). "Modeling soil water dynamics in a forested ecosystem.1. A site specific evaluation," *Hydrological Processes*, 6(4): 435-444.
- Durocher, M.G. (1990). "Monitoring spatial variability of forest interception," *Hydrological Processes*, 4(3): 215-229.
- Ford, E.D. and Deans, J.D. (1978). "Effects of canopy structure on stemflow, throughfall and interception loss in a young Sitka spruce plantation," *Journal of Applied Ecology*, 15(3): 905-917.
- Keim, R.F., Tromp-van Meerveld, H.J. and McDonnell, J.J. (2006). "A virtual experiment on the effects of evaporation and intensity smoothing by canopy interception on subsurface stormflow generation," *Journal of Hydrology*, 327(3-4): 352-364.
- Liang, W.-L., Kosugi, K., Hayashi, Y. and Mizuyama, T. (2006). "Methods for determining soil hydraulic parameters related to vertical rainwater infiltration," *Journal of the Japan Society of Erosion Control Engineering*, 59(3): 3-12. (In Japanese, with English abstract)
- Liang, W.-L., Kosugi, K. and Mizuyama, T. (2007). "Heterogeneous soil water dynamics around a tree growing on a steep hillslope," *Vadose Zone Journal*, 6(4): 879-889.
- Liang, W.-L., Kosugi, K. and Mizuyama, T. (2009). "A three-dimensional model of the effect of stemflow on soil water dynamics around a tree on a hillslope," *Journal of Hydrology*, 366(1-4): 62-75.
- Mukhlisin, M., Kosugi, K., Satofuka, Y. and Mizuyama, T. (2006). "Effects of soil porosity on slope stability and debris flow runout at a weathered granitic hillslope," *Vadose Zone Journal*, 5(1): 283-295.
- Sammori, T. and Tsuboyama, Y. (1990). "Study on method of slope stability considering infiltration phenomenon," *Journal of the Japan Society of Erosion Control Engineering*, 43(4): 14-21. (In Japanese, with English abstract)
- Suzuki, M. (1991). "Functional relationships on the critical rainfall triggering slope failures," *Journal of the Japan Society of Erosion Control Engineering*, 43(6): 3-8. (In Japanese, with English abstract)